ELSEVIER
Available online at www.sciencedirect.com
SCIENCE DIRECT®
Thermochimica Acta 438 (2005) 192–201
thermochimica acta
www.elsevier.com/locate/tca

Influence of accuracy of thermal property data of a phase change material on the result of a numerical model of a packed bed latent heat storage with spheres

C. Arkar*, S. Medved

University of Ljubljana, Faculty of Mechanical Engineering, Aškerčeva 6, 1000 Ljubljana, Slovenia

Received 14 March 2005; received in revised form 16 August 2005; accepted 28 August 2005
Available online 7 October 2005

Abstract

With the integration of latent-heat thermal energy storage (LHTES) in building services, solar energy and the coldness of ambient air can be efficiently used to reduce the energy used for heating and cooling and to improve the level of living comfort. For this purpose, a cylindrical LHTES containing spheres filled with paraffin was developed. For the proper modelling of the LHTES thermal response the thermal properties of the phase change material (PCM) must be accurately known. This article presents the influence of the accuracy of thermal property data of the PCM on the result of the prediction of the LHTES's thermal response. A packed bed numerical model was adapted to take into account the non-uniformity of the PCM's porosity and the fluid's velocity. Both are the consequence of a small tube-to-sphere diameter ratio, which is characteristic of the developed LHTES. The numerical model can also take into account the PCM's temperature-dependent thermal properties. The temperature distribution of the latent heat of the paraffin (RT20) used in the experiment in the form of apparent heat capacity was determined using a differential scanning calorimeter (DSC) at different heating and cooling rates. A comparison of the numerical and experimental results confirmed our hypothesis relating to the important role that the PCM's thermal properties play, especially during slow running processes, which are characteristic for our application.

Keywords: Latent-heat thermal energy storage (LHTES); Phase change material (PCM); Differential scanning calorimeter (DSC); Apparent heat capacity; Packed bed; Numerical model

1. Introduction

The fact that in Europe more than 40% of end energy is used in buildings has, in recent years, stimulated numerous activities, political and professional, in the area of sustainable development. In the first group of activities one can place the EU Directive on the Energy Performance of Buildings, which encourages energy-efficient building design and the greater use of natural and renewable energy sources for heating, ventilation and cooling. The second group includes R&D on advanced materials, technologies and systems, which includes latent-heat thermal energy storage (LHTES) in building services. The advantages of LHTES in comparison with sensible storage are a greater density of stored energy and a narrow operational temperature range. Recently, the performance of LHTES in systems for building heating using solar energy or for natural cooling of building has been studied by several authors [1–7].

In these studies, different Phase change materials (PCMs) were used. PCM selection depends on many factors, of which the most important are the PCM's useful life and the long-term stability, because LHTES in mentioned applications operate on daily cycles. Selection also depends on the phase change temperature, which must be suitable for the application. The next most important parameter is the price, which has an influence on the economics of the system. Commercially available materials with acceptable prices are mostly paraffins and salt hydrates. A list of commercially available materials can be found in the review article of Zalba et al. [8].

A characteristic of most paraffins and salt hydrates is that the phase change occurs in a temperature range rather than at a constant temperature, as would be expected for pure substances. An assumption that the melting or solidification occurs at constant temperature leads to a great discrepancy between experimental and numerical results [9]. For the mathematical modelling of a

---

* Corresponding author. Tel.: +386 1 4771316; fax: +386 1 2518567.
E-mail address: ciril.arkar@fs.uni-lj.si (C. Arkar).

0040-6031/$ – see front matter © 2005 Elsevier B.V. All rights reserved.
doi:10.1016/j.tca.2005.08.032

Nomenclature

a_p	superficial particle area per unit bed volume (m^{-1})
Bi	Biot number
c_{app}	apparent heat capacity of PCM (J/(kg K))
c_p	specific heat of heat transfer fluid (J/(kg K))
c_{ps}	specific heat of liquid or solid PCM (J/(kg K))
d	sphere diameter (m)
L	LHTES length (m)
L	latent heat of melting or solidification (J/kg)
m_{PCM}	mass of PCM in DSC instrument (kg)
p	pressure (Pa)
q	heat flow (W)
r	radial coordinate (m)
R	LHTES radius (m)
Re	Reynolds number
t	time (s)
T	temperature (°C)
T_a	LHTES ambient temperature (°C)
u	velocity (m/s)
U_w	overall wall heat transfer coefficient
x	axial coordinate (m)
Greek letters	
α	heat transfer coefficient ($W/(m^2 K)$)
ε	bed porosity
η	dynamic viscosity (Pa s)
ρ	density (kg/m^3)
θ	heating or cooling rate (K/min)
Θ	PCM temperature (°C)
λ_f	effective thermal conductivity in the radial or axial direction (W/(m K))
λ_{PCM}	thermal conductivity of PCM (W/(m K))

LHTES thermal response, the enthalpy function or the apparent heat capacity of the PCM has to be known; this takes into account the temperature range over which the phase transition occurs under real operating conditions.

For an apparent heat capacity representation, approximate values are often used in the models describing experimentally obtained values for the latent heat of melting or the solidification of the PCM under investigation.

Farid et al. [10] compared several different simple functions for apparent heat capacity to describe the variation of the PCM's specific heat with temperature. A simple symmetrical and asymmetrical piecewise linear function and a step function were used. The starting and ending temperatures were slightly different in each case, but the peak temperature remained the same. The area of the triangle or rectangle was equal to the latent heat of the PCM. The best agreement in the prediction of the solid/liquid interface motion in a test cell filled with paraffin was achieved when the asymmetrical triangular shape of an apparent heat capacity function was used.

The same approach, using a step function for the apparent heat capacity of a PCM, was used by Beasley et al. [11] in a numerical calculation for a packed bed LHTES. Goncalves and Probert [12], for example, used a symmetrical rational function for the specific heat approximation.

The shape of the apparent heat capacity function depends significantly on the heating and cooling rates used in the measurements. Frequently, the enthalpy function or the apparent heat capacity of the PCM is determined on the basis of DSC measurements made at too high heating/cooling rates.

Nagano et al. [13] used an approximate mean value of the enthalpy function of melting and solidification determined with DSC measurements at heating/cooling rates of 5 and 1 K/min for mathematical modelling of a packed bed heat storage with paraffin granules.

Lamberg et al. [14] used commercially available paraffin in their experiments. The material properties were determined using differential scanning calorimeter (DSC) measurements with a heating/cooling rate of 2 K/min. In mathematical simulations, the apparent heat capacity function with a rectangular shape and a large and narrow temperature range were used. The wider interval was 7 K during melting and 5 K during PCM solidification, with different starting and ending temperatures. The second function was 2 K wide, with the same starting and ending temperatures. From their results they conclude that the best agreement for the measured and modelled data is obtained when using an apparent heat capacity with a narrow temperature range. They also conclude that the material properties of the PCM should be well known in order to obtain sufficiently accurate results with numerical methods. From the figure that presents from DSC measurement calculated apparent heat capacity and the approximations used in the simulations, it is also evident that the temperature range of the narrower function was shifted from the peak temperature of the DSC measurement.

Latent heat storage in building materials was studied by Feldman and Banu [15] using DSC measurements at a heating/cooling rate of 2 K/min and at a rate that is closer to the actually experienced rate during measurements of 0.2 K/min. From the obtained results they conclude that there is no significant difference between each test. There is actually no difference in the overall latent heat, but one can see from the DSC curves that the peak temperatures differ by roughly 1 K for each process.

Based on our previous work on the agreement of the numerical model with experiments [2,9], which we made with a packed bed LHTES, we found that one of the most influential parameters is the apparent heat capacity, the shape of which depends on the heating/cooling rate. This includes the real shape of the apparent heat capacity function, the use of different functions during melting and solidification as well as considering the change in the shape and the shift of the peak temperature in terms of the actual melting/solidification rate. In the works of other authors, the actual heating or cooling rates were not taken into account or they used simplified functions. Based on this, we incorporated into a numerical model of LHTES with spheres a polynomial function for the apparent heat capacity, which was determined with least-squares fits to data from DSC measurements.

2. Apparent heat capacity of the PCM

Among possible inorganic and organic materials, paraffins were used in many applications. They are chemically and thermally stable, they are not corrosive and they show a negligible supercooling effect [8]. Their main disadvantages are their flammability and low thermal conductivity. Commercially available paraffins are mostly mixtures of different alkanes. They are cheap and available with different melting temperatures, which mean they can meet the requirements of the desired application. For our packed bed LHTES used for natural heating and cooling in a low-energy house we used RT20 paraffin from Rubitherm GmbH.

The thermal properties of RT20 paraffin were determined using DSC measurements for a heating and cooling cycle at different heating and cooling rates (5, 1 and 0.1 K/min). Fig. 1 shows an example of a DSC measurement at a heating rate of 5 K/min. The measured heat flow signal represents the difference between the heat flows of the reference calorimeter and the measured sample of PCM. From the heat flow signal five characteristic temperatures can be determined [16,17]. The onset, T_{on}, and endset, T_{end}, temperatures are the temperatures where the DSC heat flow curve separates from the base line. The extrapolated starting temperature, T_{s}, and the extrapolated ending temperature, T_{e}, are the temperatures at the intersection of the base line and the tangents at the inflection points of the DSC curve on both sides of the peak temperature, T_{p}, which is the temperature at the peak of the DSC curve.

From the measured heat flow, the apparent heat capacity is calculated using the following equation:

$$c_{\mathrm{app}}(T)=\frac{q(T)}{m_{\mathrm{PCM}}\theta}+c_{\mathrm{ps}} \tag{1}$$

where m_{PCM} is the mass of PCM used in the DSC, θ the heating or cooling rate of the DSC measurement and c_{ps} is

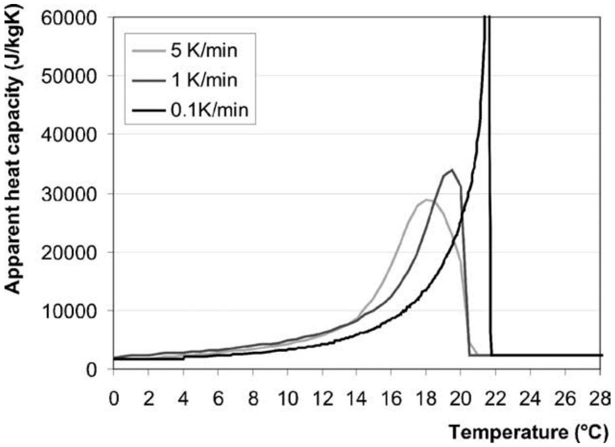

Fig. 2. Apparent heat capacity of the solidification process determined from DSC measurements at different cooling rates.

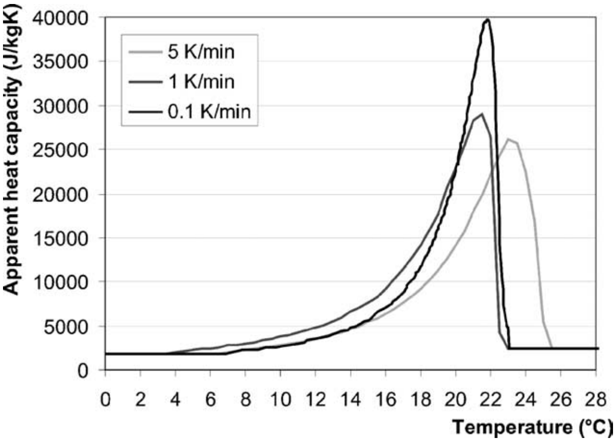

Fig. 3. Apparent heat capacity of the melting process determined from DSC measurements at different heating rates.

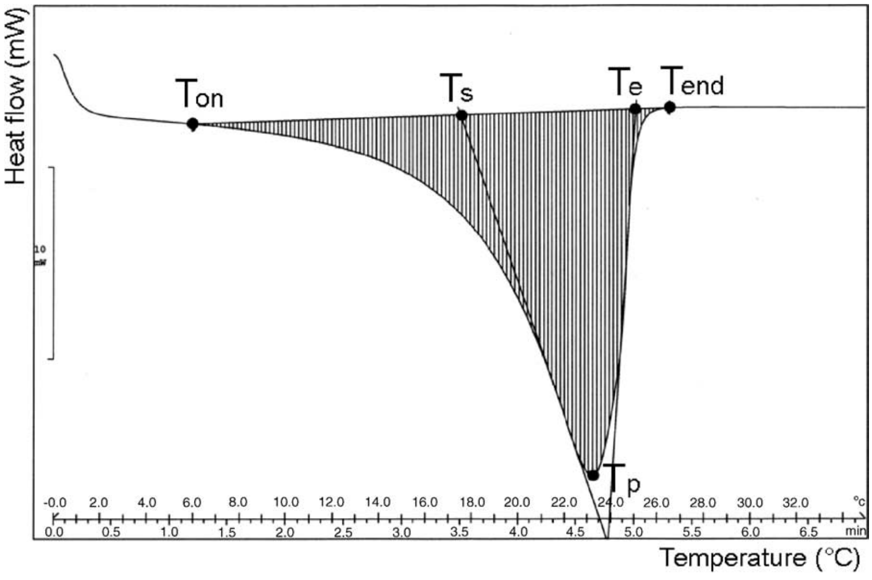

Fig. 1. DSC melting curve of RT20 paraffin at a heating rate of 5 K/min (the characteristic temperatures are indicated in the figure).

Table 1
Characteristic values determined from DSC measurements: (a) during solidification and (b) during melting

	L (kJ/kg)	T_{on} (°C)	T_{s} (°C)	T_{p} (°C)	T_{e} (°C)	T_{end} (°C)
(a) Cooling rate (K/min)						
5	144.3	22.0	21.6	18.1	115	−2.0
1	144.6	21.3	20.6	19.7	15.9	−3.0
0.1	143.4	21.8	21.7	21.5	21.1	2.9
(b) Heating rate (K/min)						
5	139.6	5.9	17.3	22.6	25.0	26.5
1	138.2	2.8	16.3	21.1	22.4	23.1
0.1	138.3	6.8	17.9	21.8	23.0	23.4

the specific heat of the solid or liquid PCM. The enthalpy of a phase change transition is obtained by integrating the first part of Eq. (1) over the transition temperature range. Figs. 2 and 3 show apparent heat capacity of RT20 paraffin obtained from the DSC measurements at heating and cooling rates of 5, 1 and 0.1 K/min. Table 1 gives the corresponding phase transition temperatures and the latent heat of melting and solidification.

From the results presented in Table 1, it can be seen that the latent heat of solidification or melting does not depend on the DSC heating/cooling rate; however, the shapes of the apparent heat capacity curves differ considerably. As observed also by other authors the shape of the DSC curve depends significantly on the heating/cooling rate and the size (mass) of the sample used in DSC [17,18]. In particular during solidification, it can be seen that the peak temperature, T_{p}, shifts towards the higher temperatures at lower cooling rates and the peak becomes narrower and higher as well, which shows that the greatest part of the latent heat evolves in a narrow temperature range. Also, the shift of the peak temperatures for both processes becomes smaller at lower heating/cooling rates. The difference between the peak temperatures of the melting and solidification processes is 3.8, 1.4 and 0.3 °C at heating/cooling rates of 5, 1 and 0.1 K/min, respectively.

3. Mathematical model of packed bed LHTES

Living comfort and energy use in buildings can be efficiently improved by using solar energy in the winter time and natural cooling in the summer time. Because of the periodic nature of solar radiation and the ambient temperature, natural heating and cooling is more effective if daily heat storage is introduced into the system to enable the accumulation of excess energy and a shift in the time of accumulated energy use. A building ventilation system with integrated, cylindrical LHTES with spheres with encapsulated paraffin has been developed for these purposes. The LHTES accumulates heat from a large-panel air solar system [19,20] during the day or the cold of ambient air during the night. Characteristically for the system's operation is the large temperature range of heat transfer fluid, and because the storage is integrated into the ducting system also a small storage to sphere diameter ratio, which results in a coupled non-uniform flow distribution over the storage cross-section.

Detailed modelling of the heat transfer and the fluid flow for individual heat storage element (for example, with CFD) in such a complex configuration would be difficult and especially because of the process dynamics also impracticable. Transient one-dimensional conduction dominated models [1,2,10,21,22] and packed bed models [4,11,12] are more commonly applied. We used an appropriately adapted packed bed model for the LHTES modelling. Ismail and Stuginsky [23] present an overview of possible packed bed models for a LHTES. The basic assumption of these models is that the spheres or PCM capsules behave as a continuous medium and not as a medium comprised of individual particles. In our case, we used a continuous solid phase model. The model forms coupled heat transfer equations for the heat transfer fluid (air):

$$\varepsilon(r)\rho c_{\mathrm{p}}\frac{\partial T}{\partial t}+u(r)\rho_{\mathrm{f}}c_{\mathrm{f}}\frac{\partial T}{\partial x}=\lambda_{\mathrm{f}x}\frac{\partial^2 T}{\partial x^2}+\lambda_{\mathrm{f}r}\left(\frac{\partial^2 T}{\partial r^2}+\frac{1}{r}\frac{\partial T}{\partial r}\right)+\alpha_{\mathrm{eff}}(r)a_{\mathrm{p}}(r)(\Theta-T) \tag{2}$$

and for the PCM:

$$(1-\varepsilon(r))\rho_{\mathrm{PCM}}c_{\mathrm{app}}(\Theta)\frac{\partial\Theta}{\partial t}=\alpha_{\mathrm{eff}}(r)a_{\mathrm{p}}(r)(T-\Theta) \tag{3}$$

The initial and boundary conditions according to Fig. 4 are:

$$\begin{array}{llllcll}
 & t=0 & & & \Rightarrow & T=\Theta=\text{const.} & \\
\text{I} & x=0; & 0\le r\le R; & t>0 & \Rightarrow & T=T(t)><T_0; & \dfrac{\partial\Theta}{\partial x}=0\\
\text{II} & r=0; & 0\le x\le L; & t>0 & \Rightarrow & \dfrac{\partial T}{\partial r}=0; & \dfrac{\partial\Theta}{\partial r}=0\\
\text{III} & x=L; & 0\le r\le R; & t>0 & \Rightarrow & \dfrac{\partial T}{\partial x}=0; & \dfrac{\partial\Theta}{\partial x}=0\\
\text{IV} & r=R; & 0\le x\le L; & t>0 & \Rightarrow & -\lambda_{\mathrm{f}r}\dfrac{\partial T}{\partial r}=U_{\mathrm{w}}(T_{\mathrm{a}}-T); & \dfrac{\partial\Theta}{\partial r}=0
\end{array} \tag{4}$$

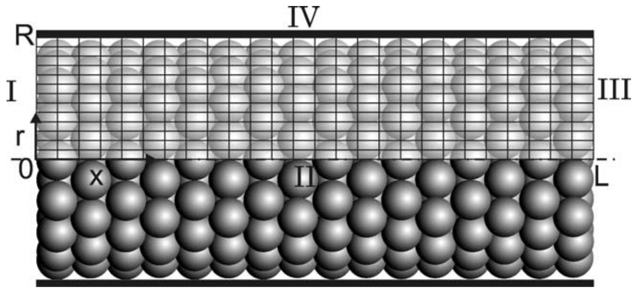

Fig. 4. Schematic representation of numerical grid and system boundaries.

Eqs. (2)–(4) were solved numerically using a finite-difference approximation [24] and the Mathematica software package. The explicit method was used. Mesh-refining techniques were used to optimise the number of mesh divisions in the axial and radial directions. In the numerical calculations, we used 40 divisions in the axial direction, 25 divisions in the radial direction and a time step of 30 s.

The distribution of the spheres in the LHTES is defined by the porosity, ε, which varies with the radial distance from the wall, in particular for a smaller tube-to-particle diameter ratio (D/d). A non-uniform radial distribution of bed porosity also influences the radial distribution of the axial fluid velocity. A monotonic exponential expression was used to represent the radial distribution of the bed porosity:

$$\varepsilon(r) = \varepsilon_\infty \left[1 + \left(\frac{0.87}{\varepsilon_\infty} - 1\right) \exp\left(-5\frac{R-r}{d}\right)\right] \tag{5}$$

where ε_∞ was selected so that the average porosity of the LHTES matched the experimentally determined porosity. The radial distribution of the axial fluid velocity was calculated using the extended Brinkman equation:

$$\frac{\partial p}{\partial x} = -A\frac{(1-\varepsilon(r))^2}{\varepsilon(r)^3}\frac{\eta}{d^2}u(r) - B\frac{1-\varepsilon(r)}{\varepsilon(r)^3}\frac{\rho}{d}u(r)^2 + \frac{\eta_{\mathrm{eff}}}{r}\frac{\partial}{\partial r}\left(r\frac{\partial u}{\partial r}\right) \tag{6}$$

The coefficients A and B were obtained from fitting experimental data. The values obtained were 310 and 0.92. The velocity gradient near the wall, as a result of wall friction, is a function of the effective viscosity, which depends on the fluid velocity. The effective viscosity is described by relations presented by Giese et al. [25]:

$$\frac{\eta_{\mathrm{eff}}}{\eta} = a\ \exp(bRe) \tag{7}$$

where for the packing of spheres $a = 2$. The coefficient b was set to 0.0018 to fit the experimental data for higher Reynolds numbers. Eq. (6) is solved using the following boundary conditions:

$$\begin{aligned} r &= 0, \quad \frac{\partial u}{\partial r} = 0 \\ r &= R, \quad u = 0 \end{aligned} \tag{8}$$

Expressions for the effective thermal conductivities in the radial and axial directions were chosen from the literature. We made use of the relations presented by Bauer and Schlunder [26], considering the actual ratio D/d for the λ_{er} calculation, and the recommended relations from Wakao and Kaguei [27] for λ_{ex}. The heat transfer coefficient between the heat transfer fluid and the solid particles in the LHTES was determined using the well-known and often used empirical correlation presented by Gnielinski [28]. Readers are referred to these articles for more details. Because of the low thermal conductivity of the PCM in the spheres, the intra-particle conduction in the spheres is considered by using the effective heat transfer coefficient [29]:

$$\alpha_{\mathrm{eff}}(r) = \frac{\alpha(r)}{1 + 0.2Bi}. \tag{9}$$

The density and the specific heat of the heat transfer fluid and the density of the PCM are assumed to be constant. For the specific heat of the PCM an apparent heat capacity approach was used to take into account the latent heat of the PCM, as described in the previous section.

4. Experimental verification

The numerical model was verified on the experimental LHTES shown in Fig. 5. The heat storage was cylindrical, with a diameter of 0.34 m; it had 35 rows of spheres structured with rhombic packing. Hollow, polyethylene spheres with a diameter of 50 mm and a wall thickness of 1 mm were filled with RT20 paraffin from Rubitherm GmbH. The height of the LHTES was 1.52 m. The packed bed's average porosity was 0.388.

Fig. 6 shows the scheme of the experimental setup. The air flow rate was measured using an orifice plate flow meter. The flow rates used in the experiments for which the basic thermal and flow characteristics were determined were between 50 and 220 m^3/h, which correspond to the flow rates used for building or room ventilation. The air was heated or cooled before it entered the mixing chamber. The air temperature at the LHTES inlet was determined using thermocouples disposed over the cross-section. The temperature and air velocity at the inlet differ only a little from the average value, so average values were used in the numerical calculations. The temperature of the air at the LHTES outlet was measured using 12 thermocouples arranged over the storage diameter. Two spheres, one in the 16th row (approximately $1/2L$) and one in the last, 35th, row (L) were equipped with three thermocouples over the sphere height for measurements of the paraffin temperature, as shown in Fig. 5.

5. Results and discussion

To show the influence of the shape of the apparent heat capacity function on the agreement between the experimental results and the results of the numerical model, four experiments are shown: two for the melting process and two for the solidification process, with a step or ramp change in the air inlet temperature. Experiments were made at different flow rates: 166 and 76 m^3/h for the solidification processes, and 108 and 215 m^3/h for the melting processes. The LHTES was isolated with a 3-cm-thick thermal isolation layer in all experiments (not shown in Figs. 5 and 6).

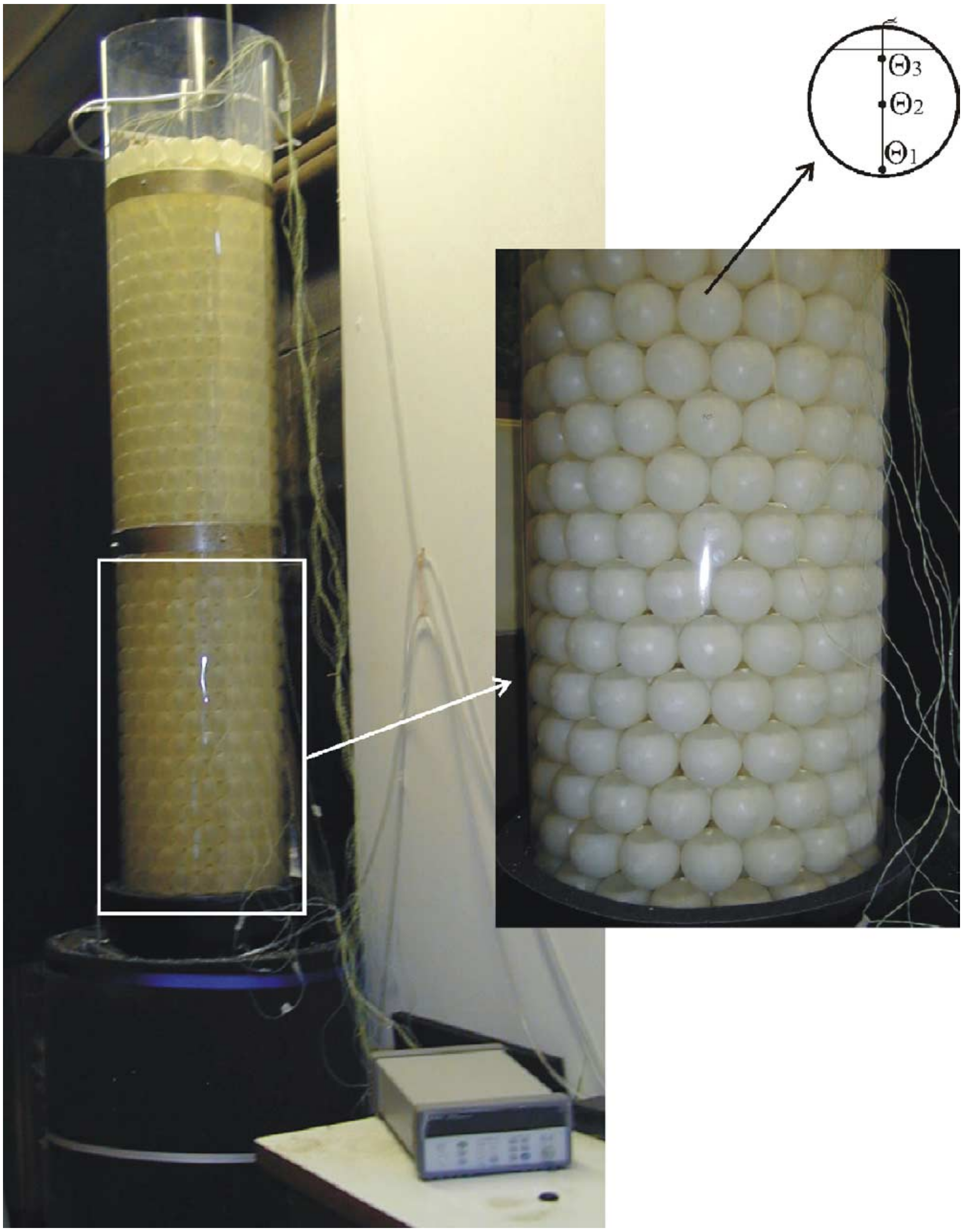

Fig. 5. Experimental LHTES; left—non-isolated cylindrical LHTES ($D = 340$ mm, $L = 1.52$ m) with PCM encapsulated in spheres ($d = 50$ mm), mixing chamber and data-acquisition unit; right—a part of the storage with PCM in spheres and a sketch of thermocouples' positions in the sphere.

5.1. Heating and cooling rates of the paraffin during experiments

The rate of PCM temperature change in the LHTES depends on the air flow rate and the temperature conditions at the storage inlet and the temperature difference between the air and the paraffin, respectively. This rate is important during the selection of an apparent heat capacity function, which should be determined based on measurements at approximately the same heating or cooling rate. Fig. 7 presents the rate of paraffin temperature change at the centre of both spheres fitted with thermocouples for the selected solidification process, which is also shown in Fig. 9A. Similarly, Fig. 8 shows the rate of paraffin temperature change for the melting process shown in Fig. 11B. The sphere in the 16th row is situated on the centreline of the

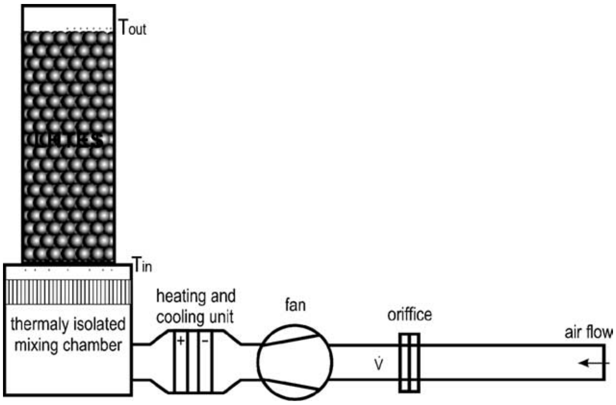

Fig. 6. Scheme of the experimental setup.

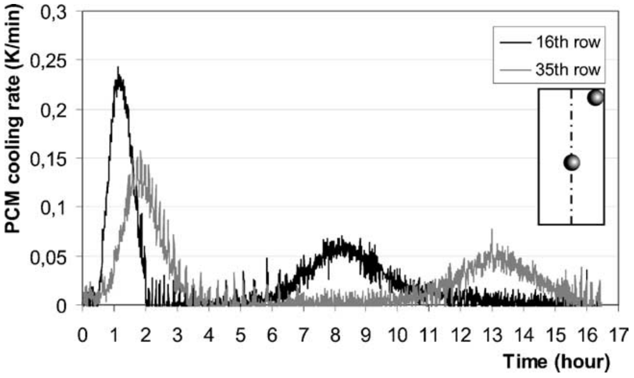

Fig. 7. Cooling rate of the PCM in spheres during the solidification process (the air flow rate is 76 m^3/h).

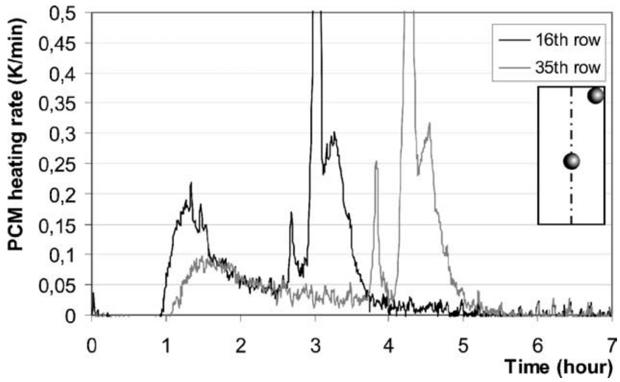

Fig. 8. Heating rate of the PCM in spheres during the melting process (the air flow rate is 215 m^3/h).

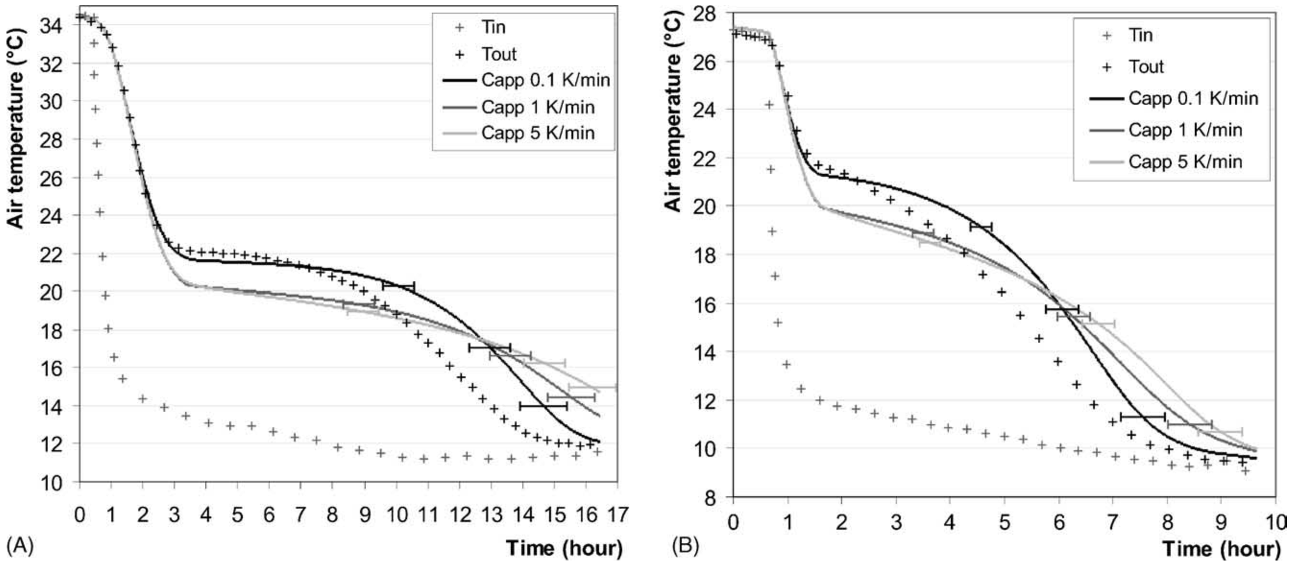

Fig. 9. Comparison of measured and modelled air temperatures at the LHTES outlet during the solidification process, the c_{app} for the solidification process is according to Fig. 2, in (A) the air flow rate is 76 m^3/h and in (B) the air flow rate is 166 m^3/h.

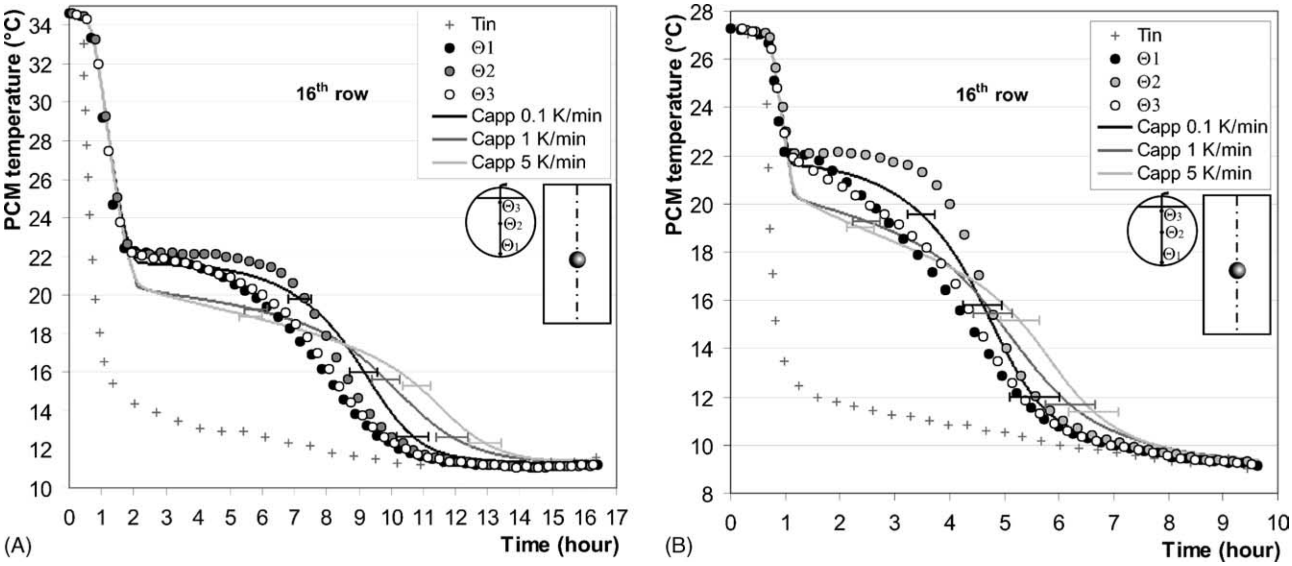

Fig. 10. Measured and modelled PCM temperatures in the solidification process: (1A) sphere in the centre of the 16th row; (2A) sphere at storage wall in the 35th row, air flow rate 76 m^3/h; (1B) sphere in the centre of the 16th row; (2B) sphere in the centre of the 35th row, air flow rate is 166 m^3/h.

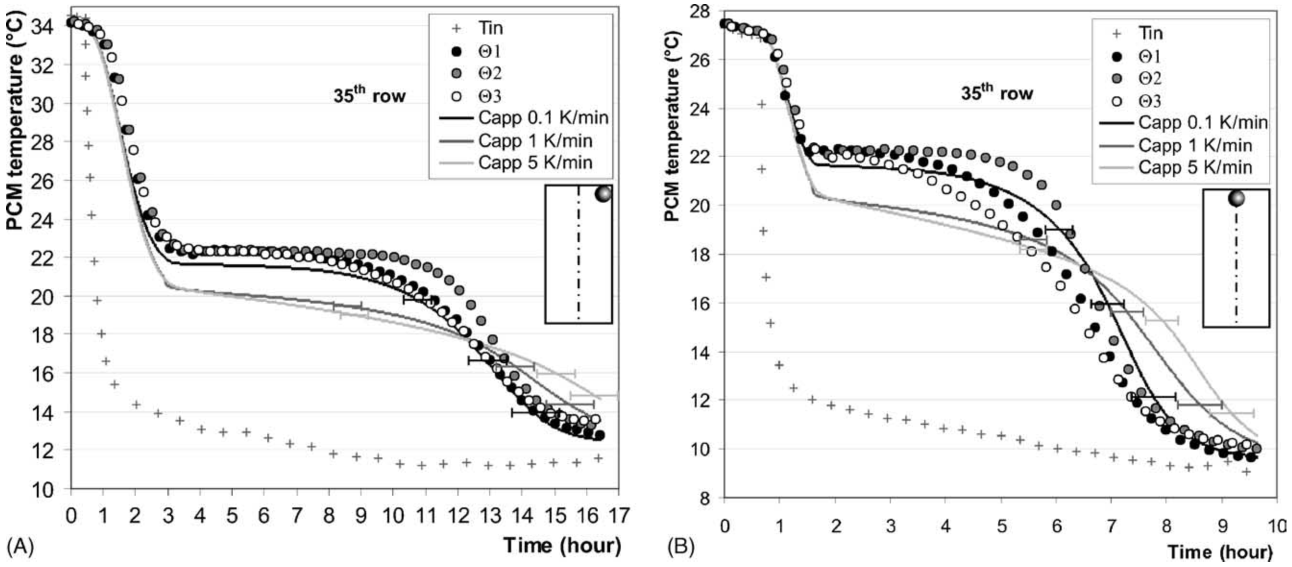

Fig. 10. (*Continued*).

bed, while the sphere in the last row is placed at the storage wall.

From Figs. 7 and 8, the shift in the start and the end of the solidification and melting processes in the monitored spheres can be observed. During the solidification process in Fig. 7, the first peak represents the sensible cooling of liquid paraffin. Then follows a period of almost constant temperature, which is close to the peak temperature. Another increase in the rate of temperature change appears when the temperature of the paraffin drops below the peak temperature and begins to approach the air temperature. During the melting process shown in Fig. 8, the first peak represents the heating of solid PCM. The rate of temperature change drops when the temperature approaches the peak temperature. A peak higher than 0.5 K/min represents the moment when the solid phase separates from the thermocouple. Because of the difference in the density of solid and liquid paraffin, the solid phase sinks to the bottom of the sphere during melting, so that the melting process is similar to the process of contact melting. The smaller peak beforehand could be described as an invasion of liquid paraffin in a pore of solid paraffin. The peak after the thermocouple separation represents the heating of liquid paraffin.

From the presented figures, it can be concluded that also at higher flow rates the rates of paraffin temperature change only slightly and for a short time exceed a value of 0.1 K/min, and that higher rates of temperature change are achieved in the rows at the LHTES inlet.

5.2. *Heating and cooling of LHTES*

Figs. 9 and 11 show the thermal response of the packed bed LHTES to a step or ramp change in the air inlet temperature. The

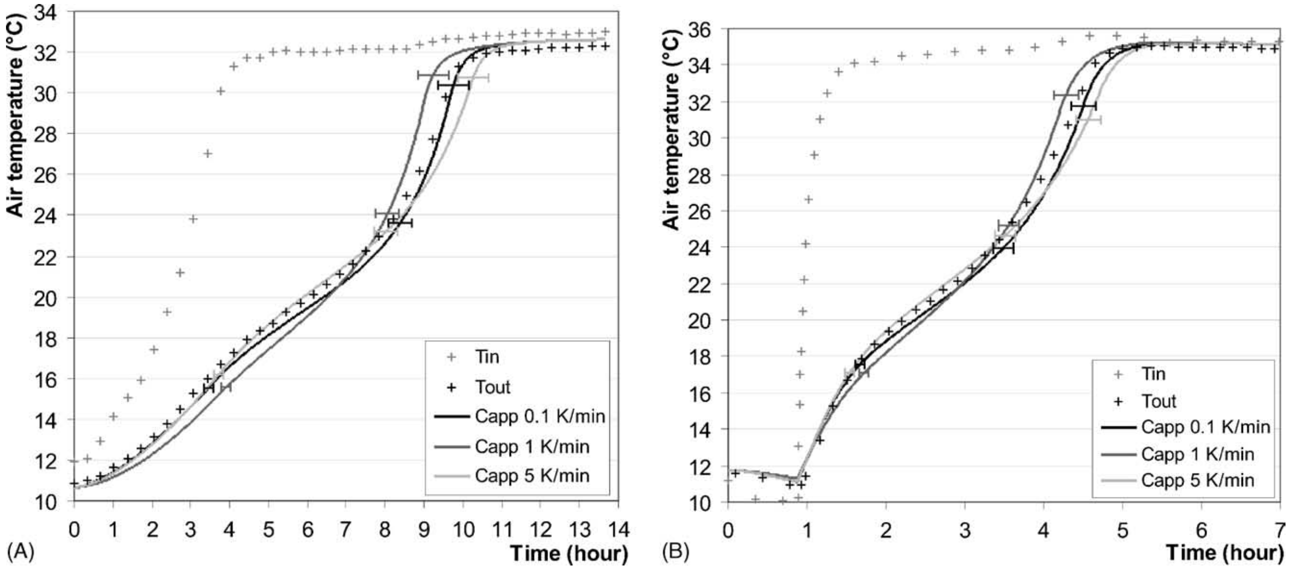

Fig. 11. Comparison of measured and modelled air temperature at the LHTES outlet during the melting process, c_{app} for the melting process is according to Fig. 3, in (A) the air flow rate is 108 $\mathrm{m^3/h}$, and in (B) the air flow rate is 215 $\mathrm{m^3/h}$.

measured air temperature at the storage inlet and at the centre of the storage outlet ($r = 0$) are shown with data points, while the numerically determined temperatures at the centre of the storage outlet are represented by the line. Each line represents numerical results for the same initial and boundary conditions but for a different polynomial function of the apparent heat capacity of paraffin determined at different heating or cooling rates. Figs. 10 and 12 show the measured and calculated temperatures of the paraffin for locations where the temperatures of the paraffin were measured. In the numerical calculations, the inlet air temperature equals the measured inlet temperature. For the air flow rate and the LHTES ambient temperature the average values for the measurement period were used.

In the experimental tests, there are errors and uncertainties associated with instrumentation and experimental procedures that have an effect on numerical results. To investigate these effects an error propagation analysis is included into numerical results presented in Figs. 9–12. The analysis includes errors and uncertainties of inlet air temperature and air flow rate. Combined standard uncertainty of air inlet temperature is ±0.3 °C and includes uncertainty in thermocouples calibration procedure and errors due to non-uniformity of inlet air temperature. Combined standard uncertainty of air flow rate is estimated to ±3% of measured air flow rate and includes uncertainty of air volume flow rate measurement and errors associated with non-uniformity of air velocity at LHTES inlet cross-section. Error bars are shown for three different temperatures of each numerical calculation for the most infavourable combination of these two uncertainties.

From the presented results, it can be seen that the best agreement between the measured and numerical results is obtained when the apparent heat capacity is calculated from DSC measurements at a heating/cooling rate of 0.1 K/min, which is the closest to the experimental conditions (as shown in Figs. 7 and 8).

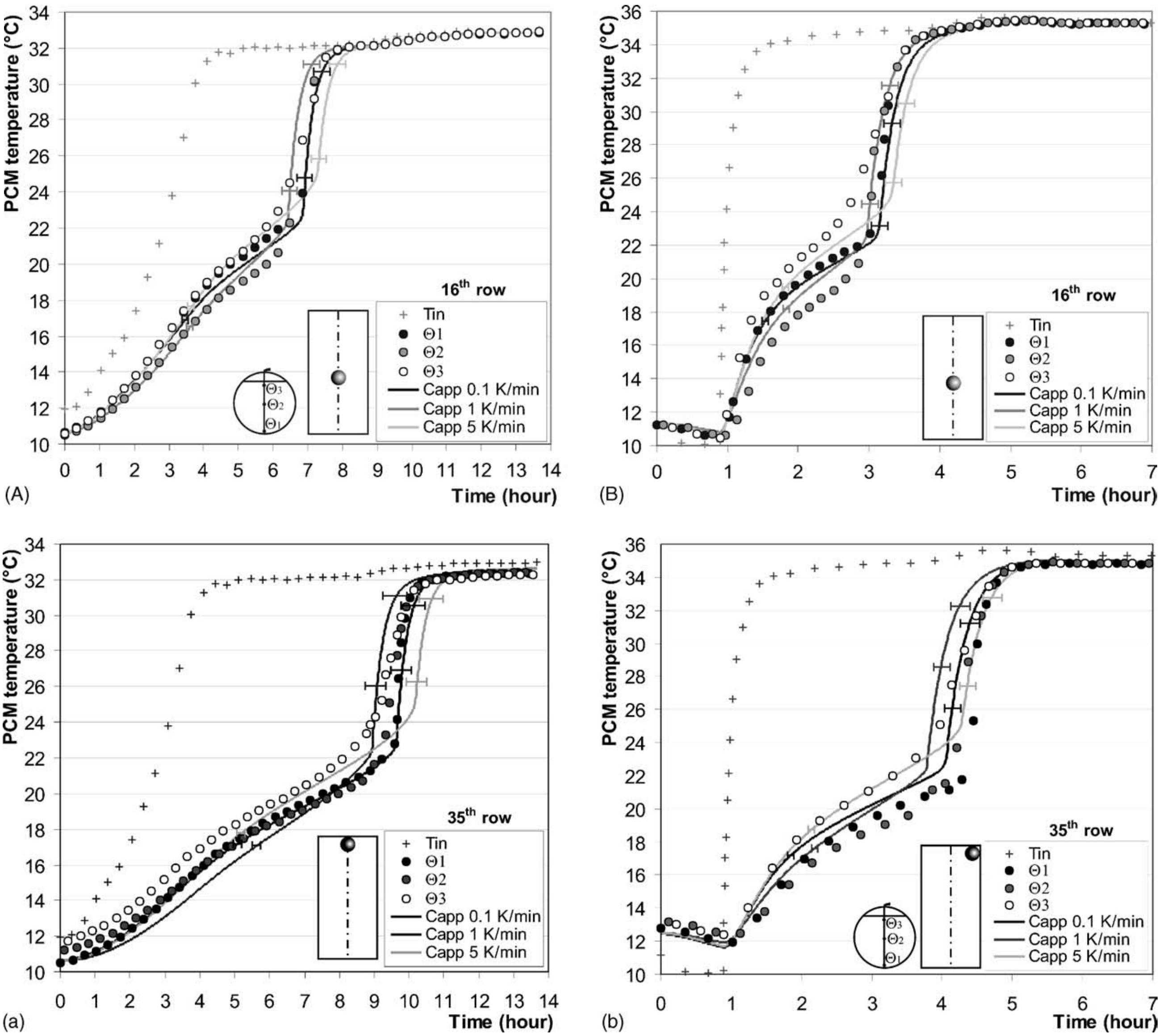

Fig. 12. Measured and modelled PCM temperatures in the melting process: (1A) sphere in the centre of the 16th row; (2A) sphere in the centre of the 35th row, air flow rate 108 m^3/h; (1B) sphere in the centre of the 16th row; (2B) sphere at storage wall in the 35th row, air flow rate is 215 m^3/h.

From Fig. 9, which shows the solidification process, the influence of the peak temperature on the agreement between the results can be seen. The air outlet temperature stays almost constant during the solidification process. This is because the shape of the apparent heat capacity function is markedly asymmetrical. When the other two functions for the apparent heat capacity, with different peak temperatures, are used, the deviation between the experimental and the numerical results is greater, and also a poorer agreement for the duration of the solidification process is achieved. Similar conclusions can be drawn from a comparison of the paraffin temperatures. In Fig. 10, all three measured temperatures and the temperatures from the numerical results for that location are shown. The best agreement is achieved when using an apparent heat capacity determined at a cooling rate of 0.1 K/min. During the melting process presented in Figs. 11 and 12, the deviations are much smaller for the temperatures and also for the duration of the process.

Error propagation analysis shows that experimental errors could not alter the conclusions drawn from Figs. 9–12 but further improvement of apparent heat capacity function is necessary. According to the measurement results, the accurate peak temperature seems to be a bit higher (Figs. 9 and 10), aproximately 22.3 °C.

6. Conclusions

In this article, we present the design and a numerical model for a cylindrical LHTES system based on spheres with encapsulated paraffin. The LHTES is integrated into the building services of a low-energy house and is used for the short-term (daily) heat or cold accumulation.

For the prediction of the LHTES system's thermal response, an adapted packed bed mathematical model was developed. The model included the radially dependent bed porosity and the fluid velocity, which was necessary because of the small tube-to-sphere-diameter ratio. A comparison of the numerical and experimental results showed that the apparent heat capacity, $c_{\text{app}}(T)$, a parameter that describes how the latent heat of the PCM evolves over the temperature range, should also include an additional influential parameter—a heating or cooling rate (θ).

Using DSC measurement results, the apparent heat capacity of the RT20 paraffin was determined for different heating and cooling rates. The obtained polynomial function, $c_{\text{app}}(T, \theta)$, for the melting and solidification was integrated into the numerical model.

In our experiments, the rate of PCM temperature change was also investigated, and it was found that for our application on average it does not exceed 0.1 K/min. Only during sensible cooling of the liquid paraffin and the sensible heating of solid paraffin did the rate of temperature change reach values of 0.2 K/min. With a comparison of the experimental and numerical results, it was proved that the agreement is considerably better when $c_{\text{app}}(T, \theta)$ is integrated into the numerical model. This is especially important for applications similar to the one presented here, where the rate of temperature change is small. The PCM's thermal properties should therefore be determined and quoted for heating and cooling rates that are similar to the actual rates of the temperature change in the application.

Unfortunately, our application does not enable an experimental verification at a higher rate of temperature change; therefore, the validity of the established function $c_{\text{app}}(T, \theta)$ could not be proved for a wider range or to verify doubts about the DSC measurements [17]. This will be the subject of our future research activities.

References

[1] W. Saman, F. Bruno, E. Halawa, Solar Energy 78 (2005) 341–349.
[2] C. Arkar, S. Medved, IEA ECES IA (Annex 17) Second Workshop, Ljubljana, Slovenia, 2002.
[3] B. Zalba, J.M. Marin, B. Sanchez-Valverde, L.F. Cabeza, IEA ECES IA (Annex 17) Third Workshop, Tokyo, Japan, 2002.
[4] S. Takeda, K. Nagano, T. Mochida, K. Shimakura, Solar Energy 77 (2004) 329–338.
[5] K. Yanbing, J. Yi, Z. Yinping, Energy Buildings 35 (2003) 417–425.
[6] K.A.R. Ismail, J.N.C. Castro, Int. J. Energy Res. 21 (1997) 1281–1296.
[7] K. Cho, S.H. Choi, Int. J. Heat Mass Transfer 43 (2000) 3183–3196.
[8] B. Zalba, J.M. Marin, L.F. Cabeza, H. Mehling, Appl. Therm. Eng. 23 (2003) 251–283.
[9] C. Arkar, M. Kavčič, S. Medved, Phase Change Material and Slurry Scientific Conference & Business Forum, Yverdon-les-Bains, Switzerland, 2003, pp. 97–106.
[10] M.M. Farid, F.A. Hamad, M. Abu-Arabi, Energy Convers. Manage. 39 (1998) 809–818.
[11] D.E. Beasley, C. Ramamarayanan, H. Torab, Int. J. Energy Res. 13 (1989) 253–265.
[12] L.C.C. Goncalves, S.D. Probert, Appl. Energy 45 (1993) 117–155.
[13] K. Nagano, S. Takeda, T. Mochida, K. Shimakura, Appl. Therm. Eng. 24 (2004) 2131–2144.
[14] P. Lamberg, R. Lehtiniemi, A.-M. Henell, Int. J. Therm. Sci. 43 (2004) 277–287.
[15] D. Feldman, D. Banu, Thermochim. Acta 272 (1996) 243–251.
[16] D. Zhang, J. Zhou, K. Wu, Z. Li, Solar Energy 78 (2005) 471–480.
[17] B. He, V. Martin, F. Setterwall, Energy 29 (2004) 1785–1804.
[18] H. Mehling, P. Schossig, IEA ECES IA (Annex 17) Eighth Workshop, Kizkalesi, Mersin, Turkey, 2005.
[19] S. Medved, C. Arkar, B. Černe, Solar Energy 75 (2003) 455–467.
[20] C. Arkar, D. Tušar, S. Medved, J. Dolinar, P. Černe, S. Štih, T. Lužnik, International Congress Energy and the Environment, vol. I, Opatija, Croatia, 2000, pp. 99–107.
[21] K.A.R. Ismail, J.R. Henriquez, Appl. Therm. Eng. 22 (2002) 1705–1716.
[22] K.A.R. Ismail, J.R. Henriquez, T.M. da Silva, Int. J. Therm. Sci. 42 (2003) 881–887.
[23] K.A.R. Ismail, R. Stuginsky, Appl. Therm. Eng. 19 (1999) 757–788.
[24] I. Plazl, M. Lakner, Uvod v modeliranje procesov, Fakulteta za kemijo in kemijsko tehnologijo, Ljubljana, 2004.
[25] M. Giese, K. Rottschafer, D. Vortmeyer, AIChE J. 44 (1998) 484–498.
[26] R. Bauer, E.U. Schlunder, Int. Chem. Eng. 18 (1978) 181–188.
[27] N. Wakao, S. Kaguei, Heat and Mass Transport in Packed Bed, Gordon and Breach, New York, 1982.
[28] V. Gnielinski, Verfahrenstechnik 12 (1978) 63–366.
[29] C.P. Jeffreson, AIChE J. 18 (1972) 409–420.